Nitrogen-doped cobalt-iron oxide cocatalyst boosting photoelectrochemical water splitting of BiVO$_4$ photoanodes

Jingyi Lin [a,c], Xiujun Han [b,*], Siyuan Liu [a], Ying Lv [a], Xin Li [d], Yixin Zhao [d], Yao Li [a], Lianzhou Wang [c], Shenmin Zhu [a,*]

[a] State Key Laboratory of Metal Matrix Composites, School of Materials Science and Engineering, Shanghai Jiao Tong University, Shanghai 200240, People's Republic of China
[b] School of Materials Science and Engineering, Qilu University of Technology (Shandong Academy of Sciences), Jinan, Shandong Province 250353, People's Republic of China
[c] Nanomaterials Centre, School of Chemical Engineering and Australian Institute for Bioengineering and Nanotechnology, The University of Queensland, QLD 4072, Australia
[d] School of Environmental Science and Engineering, Shanghai Jiao Tong University, Shanghai 200240, People's Republic of China

ARTICLE INFO

ABSTRACT

Photoelectrochemical water splitting using bismuth vanadate (BiVO$_4$) photoanodes is of special interest for solar energy utilization. However, its solar-to-hydrogen conversion efficiency is hindered by unfavorable surface reaction kinetics, which requires the development of efficient cocatalysts. Here, a nitrogen-doped cobalt-iron oxide (N-CFO) cocatalyst layer is designed on the BiVO$_4$ (BVO) by using Prussian blue analogue (PBA) precursor. The N-CFO/BVO photoanode exhibits an improved photocurrent density of 4.83 mA/cm^2 at 1.23 V *vs.* reversible hydrogen electrode under AM 1.5 G illumination, which is 4.13-fold that of pure BVO photoanode and surpasses that of CFO/BVO with oxygen vacancies. Mechanism studies reveal that compared with oxygen vacancies, nitrogen dopants greatly enhance electrical conductivity and boost reaction activity of cobalt-iron oxide. Owing to the diverse composition of PBAs, this work provides a novel insight into the effects of nitrogen dopants, as well as a general strategy to design efficient and cheap cocatalysts for photoanodes.

1. Introduction

Photoelectrochemical (PEC) water splitting is regarded as a promising strategy to mitigate current energy and environment issues because it utilizes solar energy to realize water-hydrogen-water cycling in a zero-emission way [1]. As known, due to its four-electron nature and sluggish kinetics, oxygen evolution reaction (OER) happened on photoanodes is the rate determining step of the water splitting and the key challenge for the development of PEC system [2,3]. Numerous recent studies have focused on the exploration of a high-performance photoanode. Among all the possible photoanode materials, monoclinic bismuth vanadate (BiVO$_4$) with appropriate band structure is the most attractive one [3–5]. BiVO$_4$ has a narrow band gap of ~2.4 eV and appropriate band edge position for water splitting [1,4], thus BiVO$_4$ photoanode is expected to reach a photocurrent density of 7.5 mA/cm^2 and a solar-to-hydrogen (STH) efficiency of 10% (under AM 1.5 G illumination)[4,6]. However, limited by its unfavorable surface water oxidation

kinetics and charge carrier recombination, the photocurrent densities of bare BiVO$_4$ photoanodes reported are still considerably lower than the theoretical maximum.

Loading cocatalysts is an effective approach to promote PEC water splitting efficiency [7]. Water oxidation cocatalysts either accelerates charge transfer at the semiconductor-electrolyte interface and inhibits the interfacial recombination [7,8], or reduces the OER energy barrier [5,9]. As a result, the photoanode coupled with cocatalyst often shows a more convex photocurrent-potential (*J-V*) curve with higher current density and lower onset potential. Generally, noble-metal-based cocatalysts exhibit highest activity, but in view of their high cost and low abundance, transition-metal-based cocatalysts are widely researched as alternatives. Since the first successful trial of the introduction of Co-Pi [10,11], various cocatalysts with Fe, Co and Ni ions as active sites have arisen continuously, such as hydroxides/oxyhydroxides [12–15], oxides [3,16]. At the pursuit of a highly-efficient cocatalyst, there are two issues to consider: (1) to accelerate the charge transportation across

the cocatalyst layer and (2) to boost the activity of catalyst centers. Defect engineering is a common strategy to improve OER performance of cocatalysts. As the most widely-studied anion defect, oxygen vacancies are easy to form and alter the electronic band structure of catalytic materials [17]. It is reported that dual metal oxides with abundant oxygen vacancies have been proven to enhanced charge carrier transfer ability and H_2O adsorption [18,19].

Apart from oxygen vacancy, nitrogen dopant is another anion defect to enhance OER kinetics. Many studies have proven that the incorporation of N atoms into transition-metal-based compounds as electrocatalysts can greatly enhance their OER performance [20,21]. As substitutional defects, N dopants induce less lattice distortion, which may cause carriers scattering. M-N bonds (M = Fe, Co, Ni, *etc.*) generally have higher electrical conductivity than M-O bonds, thus endow transition metal oxides metallic characteristic [22,23]. On the other hand, N doping modulates the electron configuration [22]. The N atoms have strong electron-withdrawing ability and enhance electron transfer from the adjacent metal atoms. Moreover, the insertion of N atoms also causes *d*-band contraction and density-of-states (DOS) change of the metal atoms [24]. Therefore, N atoms doping is supposed to be a promising method to obtain highly-active cocatalyst. However, cocatalysts with N doping has been rarely reported in PEC water splitting because its preparation generally needs highly reductive ammonia gas (NH_3) as N source [21,25], which corrodes light-harvesting semiconductor (*i.e.*, $BiVO_4$) and damages the overall performance.

As known, Prussian blue analogues (PBAs) with a chemical formula of $M_3[M'(CN)_6]_2 \cdot nH_2O$ (M and M' represent transition metal elements, *e.g.*, Co^{2+}, Fe^{2+}, Fe^{3+}, Ni^{2+}, *etc.*) have great diversity of chemical composition [26] and are excellent precursors to prepare metal oxides, alloys and other nanomaterials for energy conversion and storage. For example, Han et al. prepared Ni-Co PBA nanocages and then transformed them to mixed oxide nanocages, demonstrating excellent OER activity with a small overpotential of 0.38 V and good durability [27]. Furthermore, as a N-rich species, PBAs are also potential precursors for N-doped nanomaterials under a mild atmosphere. Hou et al. fabricated novel N-doped porous $Fe/Fe_3C@C$ nanoboxes under an Ar airflow using graphene oxide (GO) and PB nanocubes as the precursors [28]. These works suggest that through appropriate synthesis method, PBAs can deposit N-doped cocatalysts with controllable thickness and composition onto $BiVO_4$ for efficient photoelectrochemical water splitting.

Herein, we report the design of a new N-doped cobalt-iron oxide cocatalyst loaded onto $BiVO_4$ photoanode through a mild and *in situ* synthesis route. CoFe PBA is selected as the precursor and annealed under the protection of N_2 atmosphere to create uniform doping of N within the cocatalyst layer. Experimental and computational studies reveal that in comparison to O vacancies, N dopants enhance both electrical conductivity and reaction activity of cobalt-iron oxide. The optimized N-CFO/BVO photoanode exhibits an enhanced photocurrent density of 4.83 mA/cm² at 1.23 V *vs.* reversible hydrogen electrode (RHE) under AM 1.5 G illumination, superior to CFO/BVO with oxygen vacancy defect and is one of the best $BiVO_4$ photoanodes modified by Co and/or Fe based cocatalyst.

2. Experimental section

2.1. Materials

All the chemicals were used without further purification. $Bi(NO_3)_3 \cdot 5 H_2O$ (99%, AR), $FeCl_3 \cdot 6 H_2O$ (99%, AR), $CoCl_2 \cdot 6 H_2O$ (99%, AR), $C_6H_5Na_3O_7 \cdot 2 H_2O$ (99%, AR) and $K_3Fe(CN)_6$ (99.5%, AR) were purchased from Sinopharm Chemical Reagent Co., Ltd. KI (99%, AR), ethanol (99.5%, AR), *p*-benzoquinone (98%, CP), dimethyl sulfoxide (99.5%, AR), vanadyl acetylacetonate (99%, AR) and NaOH (96%, AR) were purchase from Shanghai Aladdin Biochemical Technology Co., Ltd.

2.2. Preparation of $BiVO_4$, N-$BiVO_4$, CFO/$BiVO_4$ and N-CFO/$BiVO_4$ electrodes

2.2.1. Synthesis of $BiVO_4$ (BVO) electrodes

$BiVO_4$ electrodes were prepared according to the previous literature [14]. Briefly, 2 mmol of $Bi(NO_3)_3 \cdot 5 H_2O$ was dissolved into 50 mL of 0.4 M KI solution and HNO_3 was dropped to adjust pH to 1.7. After completely dissolved, this solution was mixed with 20 mL of ethanol solution of 0.5 g of *p*-benzoquinone and then was vigorously stirred for 2 h. A three-electrode cell was used for electrodeposition with a piece of fluorine-doped tin oxide (FTO) substrate working electrode, Ag/AgCl (saturated KCl) reference electrode and platinum counter electrode. The electrodeposition process was performed on an electrochemical workstation (CHI660E, CH Instruments, Inc.) at −0.1 V *vs.* Ag/AgCl for 5 min to obtain BiOI film. 70 μL of dimethyl sulfoxide (DMSO) solution of 0.2 M vanadyl acetylacetonate (VO(acac)$_2$) was dropped onto the BiOI film. The electrodes were transferred to a muffle furnace and annealed at 450 ℃ for 2 h with a ramping rate of 5 ℃/min. After cooling to room temperature, the electrodes were soaked in 1 M NaOH solution for 30 min to remove excess V_2O_5. Finally, the $BiVO_4$ electrodes were rinsed with D.I. water and dried in the air.

2.2.2. Electrodeposition of CoFe PBA on BVO electrodes

Typically, 0.1351 g $FeCl_3 \cdot 6 H_2O$, 0.2159 g $CoCl_2 \cdot 6 H_2O$, 0.125 g $C_6H_5Na_3O_7 \cdot 2 H_2O$ and 0.3293 g $K_3Fe(CN)_6$ were dissolved into 50 mL of D.I. water. The electrodeposition was conducted at 0.4 V *vs.* Ag/AgCl for 60 s. The resulting PBA/BVO electrodes were rinsed with D.I. water and dried in the air.

2.2.3. Synthesis of N-CFO/BVO, CFO/BVO and N-BVO electrodes

The PBA/BVO and BVO electrodes were annealed at 350 ℃ for 2 h under N_2 flow in a tube furnace. The obtained samples were denoted as N-CFO/BVO and N-BVO, respectively. The CFO/BVO electrodes were prepared by annealing PBA/BVO electrodes at 350 ℃ for 2 h in a muffle furnace.

2.3. Photoelectrochemical measurements

The PEC measurements were performed on an electrochemical workstation (CHI660E, CH Instruments, Inc.) using a three-electrode cell with Ag/AgCl (saturated KCl) and Pt foil as reference and counter electrodes, respectively. A 300 W Xe lamp (CEL-HXUV300, CEAULIGHT Co. Ltd., China) coupled with an AM 1.5 G filter was used as the light source from the back side of the samples and the light intensity was calibrated to 100 mW/cm² by a photoradiometer (PL-MW 2000, Perfectlight Technology Co. Ltd.). 1 M potassium borate (pH 9.7) was used as the electrolyte. All the potentials *vs.* RHE were converted from potentials *vs.* Ag/AgCl according to the following equation: $E_{RHE} = E_{Ag/AgCl} + 0.059 \times pH + E^0_{Ag/AgCl}$ ($E^0_{Ag/AgCl} = 0.197\ V$ at 25 ℃).

Photocurrent (*J*)- potential (*V*) curves were measured by linear sweep voltammetry method with applied voltage of 0.3–1.7 V_{RHE} and a scan rate of 10 mV/s. The experimental photocurrent density can be expressed as:

$$J_{H_2O} = J_{max} \times \eta_{LH} \times \eta_{trans} \times \eta_{sep} \qquad (1)$$

where J_{max} is the theoretical maximum photocurrent density (~7.5 mA/cm² for $BiVO_4$), η_{LH}, η_{trans} and η_{sep} represent the efficiency of light harvesting, charge transfer and charge separation, respectively. To calculate the surface charge transfer efficiency (η_{trans}), *J-V* curves were also measured in a 1 M potassium borate electrolyte with 0.2 M Na_2SO_3 (pH 9.7). η_{trans} can be calculated as $\eta_{trans} = \frac{J_{H_2O}}{J_{Na_2SO_3}}$, where J_{H_2O} and $J_{Na_2SO_3}$ are the photocurrent densities obtained in 1 M potassium borate electrolyte without and with 0.2 M Na_2SO_3.

Incident photon-to-current efficiency (IPCE) was obtained by

combining a monochromator (GLORIA-X500A, Zolix Co. Ltd., China) coupled with a 500 W Xe lamp (CEL-S500, CEAULIGHT Co. Ltd., China). Photocurrent was measured at 1.23 V_{RHE} under variable wavelength and the corresponding light intensity was measured by an optical power meter (CEL-NP2000, CEAULIGHT Co. Ltd., China). IPCE values were calculated by formula: IPCE $= \frac{J \times 1240}{\lambda \times P_{light}} \times 100\%$. EIS was measured with an amplitude of 5 mV and AC potential frequency range of 0.01 Hz–10 kHz at the open circuit potential in the dark. Mott-Schottky analysis was performed by sweeping the range of 0.1–0.8 V_{RHE} with an AC frequency of 1 kHz and an amplitude of 5 mV under dark condition. The donor concentration can be calculated by the following equation:

$$N_d = \left(\frac{2}{e \varepsilon \varepsilon_0} \right) \left[\frac{d(1/C^2)}{dV} \right]^{-1} \tag{2}$$

where ε_0 is vacuum permittivity, ε is relative permittivity (68 for BiVO$_4$), C is the capacitance of the space charge region and V is the applied potential [3].

The gas evolution of H$_2$ and O$_2$ was measured in an air-tight cell at 0.8 V_{RHE} under AM 1.5 G illumination and the amounts of gases were detected by a gas chromatograph (Shimadzu GC-2014C, argon as a carrier gas) with a PLS-SXE300 Labsolar-6A closed gas-circulation system (Perfectlight, China). The Faradaic efficiency was calculated as:
Faradaic efficiency $= \frac{amount\ of\ H_2\ evolution}{theoretical\ amount\ of\ H_2\ evolution} \times 100\%$.
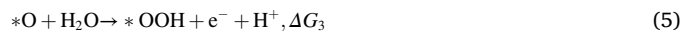
2.4. Characterization

The morphology of the electrodes was characterized by scanning electron microscopy (SEM, JSM-6360LV) and transmission electron microscopy (TEM, JEM-2010HT). XRD patterns of the samples were recorded on a Rigaku D/max 2550VL/PC system, using Cu Kα radiation. Fourier transform infrared (FT-IR) spectra were obtained by a Thermo Scientific Nicolet 6700 spectrometer. X-ray photoelectron spectra (XPS) were collected on an Thermo Scientific K-Alpha X-ray photoelectron spectrometer with an Al Kα ($hv = 1486.8$ eV) radiation source. All of the binding energy was calibrated with C 1s (284.8 eV) as reference. Raman spectra were measured at room temperature using a Renishaw inVia spectrometer. A 532 nm He-Ne laser was used as the excitation source. UV-Visible (UV-Vis) absorption spectra were recorded by a PerkinElmer Lambda 750S UV-Vis-NIR spectrophotometer. The contact angle (CA) was recorded by a Drop Shape Analyzer system (DSA100, KRÜSS, Germany).

2.5. Computational details

All the calculations were conducted by density functional theory (DFT) methods in the Vienna *ab initio* simulation package (VASP) [29]. The generalized gradient approximation (GGA) of the Perdew-Burke-Ernzerhof (PBE) functional with a Hubbard correction (PBE+U), which accounts for the Coulomb interaction of localized *d*-electrons, was applied to describe the exchange-correlation potential. Following the Materials Project online database, in this study the U_{eff} values of 5.3 eV for Fe and 3.32 eV for Co were applied. The energy cutoff for plane-wave expansion was 520 eV. The geometry configurations were optimized by the convergence criteria of 1×10^{-5} eV and 0.03 eV/Å for the electronic energy and force. The vacuum space was set to be 15 Å to avoid interactions between periodic slabs. CoFe$_2$O$_4$ slab was established by cutting the (100) surface of bulk CoFe$_2$O$_4$, which contains 56 atoms, and Co atom is selected as adsorb site. In the calculations, the electronic spin polarization was always considered, and the Brillouin zone of the slab was sampled using Γ-centered k-point mesh of $6 \times 6 \times 1$.

The oxygen evolution reaction (OER) process can be divided into four steps:

$$* + H_2O \rightarrow *OH + e^- + H^+, \Delta G_1 \tag{3}$$

$$*OH \rightarrow *O + e^- + H^+, \Delta G_2 \tag{4}$$

$$*O + H_2O \rightarrow *OOH + e^- + H^+, \Delta G_3 \tag{5}$$

$$*OOH \rightarrow O_2 + * + e^- + H^+, \Delta G_4 \tag{6}$$

where "* " refers to an active site on the catalyst and *O, *OH and *OOH are adsorbed intermediates.

The Gibbs free energy for OER process was calculated as $\Delta G = E_{abs} + \Delta E_{ZPE} - T\Delta S + \Delta U(0 \rightarrow T)$, where E_{abs}, ΔE_{ZPE} and ΔS are the adsorption energy of intermediate, zero-point energy and entropy of the reaction, respectively. and ΔU is the energy difference from 0 K to the temperature T. The thermal correction for adsorbate was calculated using the package VASPKIT [30]. The overpotential is defined as $\eta = max\{\Delta G_1, \Delta G_2, \Delta G_3, \Delta G_4\}/e - 1.23V$.

## 3. Results and discussion

3.1. Preparation and characterization of photoanodes

The BiVO$_4$ electrodes (BVO) were first prepared by the literature-reported method and the as-synthesized BVO films show a typical nanoporous morphology [13,14] (Fig. S1(a), Supporting Information). The subsequent treatment is shown in Scheme 1. In order to obtain a nitrogen-doped oxide cocatalyst, we employed Prussian blue analogue (CoFe PBA) as a N-rich precursor instead of hydroxides or oxyhydroxides used in most literatures [31,32], in which Co and Fe atoms are connected by cyano groups and form a framework. PBAs can be electro-deposited onto BiVO$_4$ photoanodes, which ensures the electrochemical contact between cocatalyst and semiconductor. The composition and thickness of the cocatalyst layer can be easily tuned by the composition of precursor solution and deposition time. In this work, metal oxide with Co and Fe dual atom ions was selected and the atomic ratio of Co to Fe in the precursor solution was controlled to be 1:2. After the electrodeposition process, the morphology in SEM image remains the same with pristine BVO electrode and XRD pattern of PBA/BVO only shows diffraction peaks from BiVO$_4$ and FTO (Fig. S1(c) and Fig. S2(a)). But in comparison with pure BVO, an ultrathin layer can be obviously observed on the surface of BiVO$_4$ in the TEM image of PBA/BVO sample (Fig. S1(b) and Fig. S1(d)) and two additional peaks at 2158 cm^{-1} and 2064 cm^{-1} appear in the Fourier transform infrared (FT-IR) spectrum (Fig. S2(b-c)), corresponding to the stretching of Co-NC-Fe species in the PBA skeleton [33,34]. After electrodeposition, blue PBA changes the color of BVO electrodes from yellow to green (Fig. S2(d)), also indicating the successful formation of PBA precursor.

The PBA/BVO electrodes were annealed in N$_2$ atmosphere and air respectively, denoted as N-CFO/BVO and CFO/BVO (Scheme 1). After that, the color of the samples is recovered, as shown in Fig. S2(d). SEM images exhibit that the nanoporous morphology of BiVO$_4$ is still maintained and there is no obvious aggregation of small particles (Fig. 1(a) and Fig. S1(e)). TEM and HRTEM images clearly reveal the successful growth of a cocatalyst layer with a thickness of 2–5 nm (Fig. 1(b-c) and Fig. S1(f)). The lattice space of 0.31 nm can be well indexed to the (121) plane of BiVO$_4$[35]. EDS mapping images in Fig. 1(d) further confirm the uniform distribution of Co and Fe elements on the surface of BiVO$_4$ nanoparticles. What's more, EDS also proves the existence of N element in the N-CFO cocatalyst layer. As shown in Fig. S2(c), after annealing, the intensity of two FT-IR peaks is weakened apparently, suggesting the breaking of Co-NC-Fe skeleton. However, protected by N$_2$ atmosphere, N atoms in cyano linker can be reserved as a doping element. The results above confirm the effectiveness of PBA deposition and calcination method to prepare a conformal and ultrathin N-doped cocatalyst layer.

Due to the low loading content, no additional peaks appear in XRD
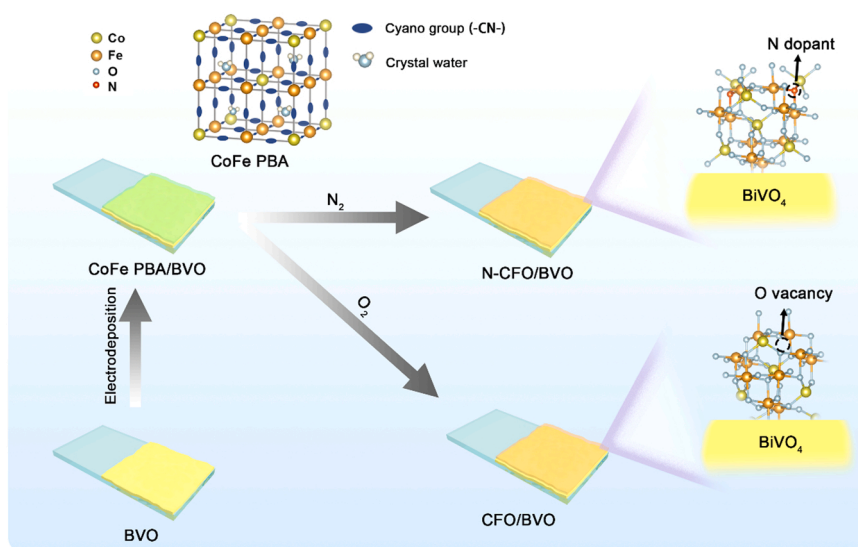
Scheme 1. Schematic illustration of the preparation of N-CFO/BVO and CFO/BVO photoanodes.
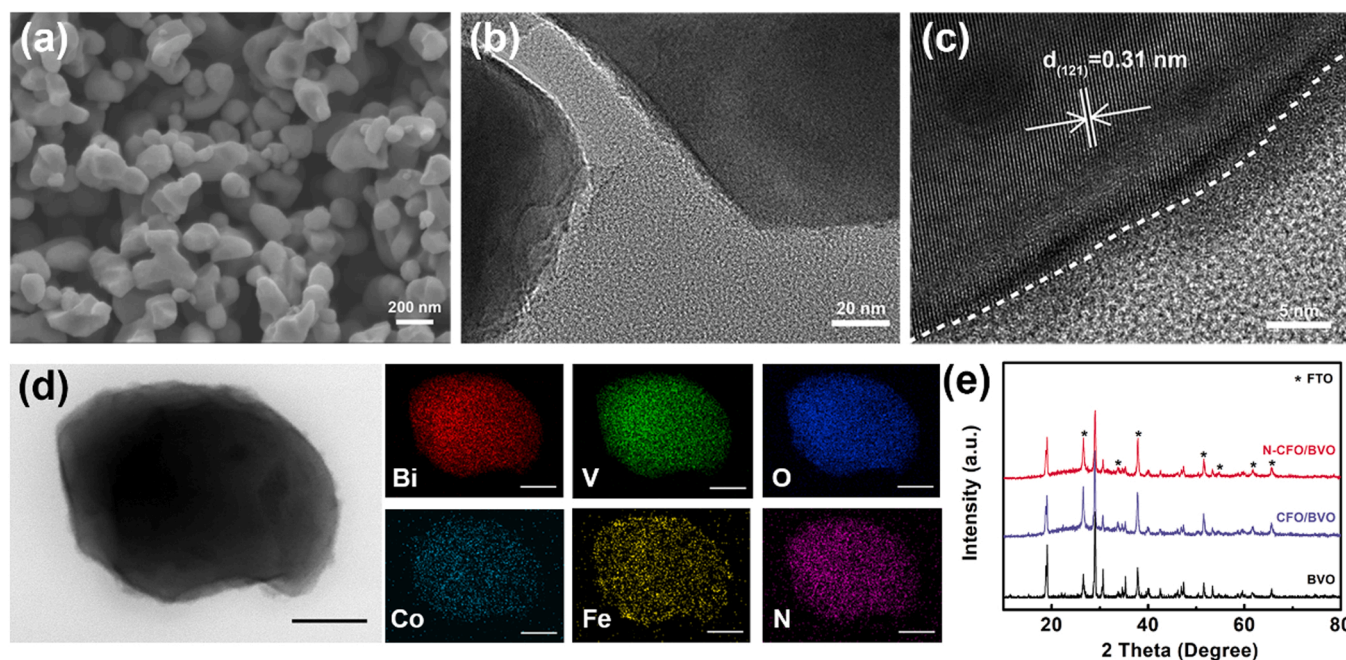

Fig. 1. (a) SEM image of N-CFO/BVO. (b) TEM image of N-CFO/BVO. (c) HRTEM image of N-CFO/BVO. (d) Energy-dispersive X-ray spectroscopy (EDS) mapping of N-CFO/BVO, scale bar: 50 nm. (e) XRD patterns of BVO, CFO/BVO and N-CFO/BVO.

patterns in Fig. 1(e), except for the diffraction peaks of monoclinic $BiVO_4$ (PDF #83–1700) and the FTO substrate (PDF #46–1088). The chemical composition of the cocatalyst layer was further investigated by X-ray photoelectron spectrometer (XPS). Compared to CFO/BVO, the N 1s spectrum of N-CFO/BVO in Fig. 2(a) further confirms the existence of N, and the peak located at 398.8 eV can be well assigned to Co/Fe-N bonds [32,36]. Note that N-CFO is declared as N-doped cobalt-iron oxide instead of nitride because it is difficult for Prussian blue analogues to form nitride directly under such condition due to the existence of crystal water [37]. The atomic ratio of (Co+Fe)/N from XPS analysis is about 1.15, which also proves the absence of metal nitride.

The O 1s spectra of N-CFO/BVO and CFO/BVO can be deconvoluted into three peaks, as shown in Fig. 2(b). The peaks at around 529.7 eV, 531.3 eV and 532.3 eV are assigned to oxygen in lattice (O_L), oxygen vacancy (O_V) and chemisorbed oxygen (O_C). An obvious peak of O_V peak

can be found in the O 1s spectrum of CFO/BVO, which indicates the existence of oxygen vacancies. Interestingly, after N_2 annealing, the ratio of oxygen vacancy (O_V) decreased from 24% to 13%, implying that N dopants occupied the original O sites. The Fe 2p and Co 2p spectra (Fig. 2(c) and (d)) are composed of two regions and the fitted peaks confirm the coexistence of Fe^{2+}/Fe^{3+} and Co^{2+}/Co^{3+} in the cocatalyst layer. The ratio of Co^{2+}/Co^{3+} in N-CFO/BVO and CFO/BVO are 1.92 and 1.69, respectively. The oxygen vacancies in CFO/BVO are generated due to the mixed valence states of Co and Fe, while in N-CFO/BVO, the incorporation of N occupies the O sites as a substitutional defect and helps to balance the valence state of Co and Fe. The increased ratio of bivalent Co (Co(II)) results from lower electronegativity of N than O. As reported previously, higher proportion of high-spin Co^{2+} may be beneficial to the oxygen evolution reaction [10], since Co atoms undergo stepwise oxidation from Co(II) to Co(III) and finally Co(IV)[38,39]. In
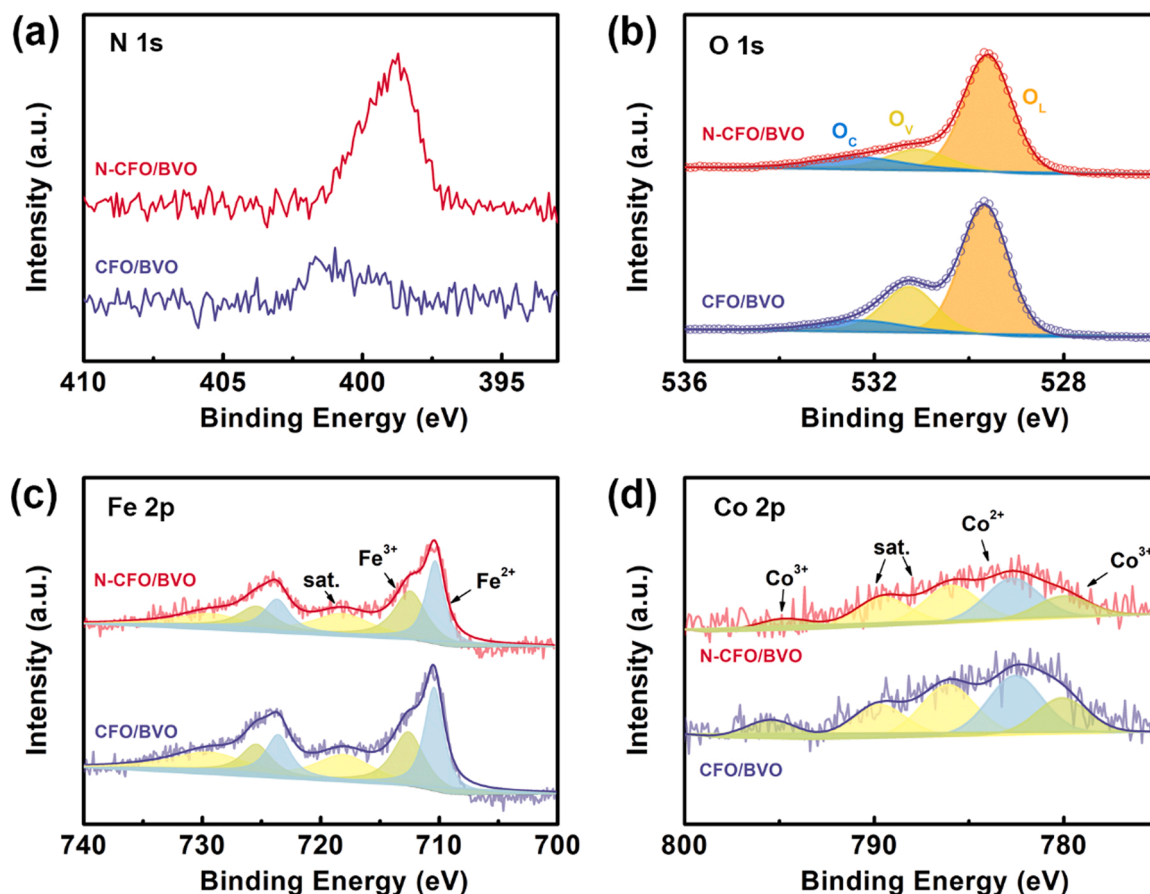
Fig. 2. High-resolution XPS spectra of N-CFO/BVO and CFO/BVO films: (a) N 1s, (b) O 1s, (c) Fe 2p and (d) Co 2p.

the high-resolution Fe 2p spectra, the peaks of N-CFO/BVO shift to lower binding energy, indicating the augment of electron density around the Fe atoms. Generally, transition metal ions serve as active center in

catalytic reactions and electron-rich atoms is more favorable [40,41]. Therefore, the valence state change of both Co and Fe in N-CFO/BVO may be beneficial to its activity.
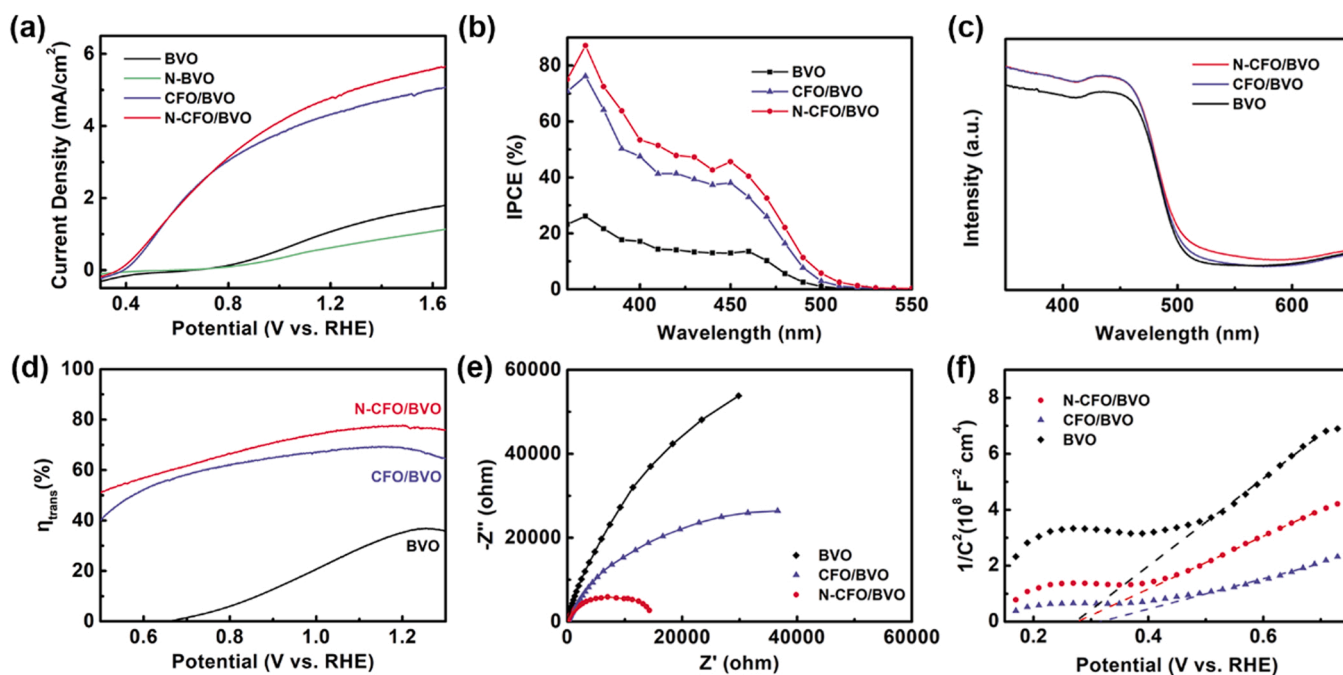

Fig. 3. (a) Photocurrent density *versus* applied potential curves of BVO, N-BVO, CFO/BVO and N-CFO/BVO. (b) IPCE curves, (c) UV-Vis spectra, (d) surface charge transfer efficiency, (e) EIS curves, and (f) Mott-Schottky plots of BVO, CFO/BVO and N-CFO/BVO.

The Bi 4f and V 2p spectra (Fig. S3(a) and (b)) show three main peaks, fitted well with Bi $4f_{5/2}$, Bi $4f_{7/2}$ and V $2p_{3/2}$ peaks in the literature [42]. Compared to BVO, the Bi4f and V2p peaks of both N-CFO/BVO and CFO/BVO are shifted to higher binding energy. This shift should not be attributed to N penetration into $BiVO_4$, since the N-doped $BiVO_4$ will show a shift to lower binding energy in Bi and V spectra because of lower electronegativity of N [43]. As shown in Fig. S4, all the Raman peaks of BVO film agree well with previous literature [44]. After the electrodeposition and secondary annealing, no peak shift is observed in Raman spectra, implying that these processes do not modify the bulk property of $BiVO_4$ and no embedment of N element. Therefore, it is believed that the peak shift in Bi and V XPS spectra results from the strong electron interaction between $BiVO_4$ and the cocatalyst layer [45].

3.2. Photoelectrochemical (PEC) water splitting performance

The PEC performance of the samples was evaluated in potassium borate buffer solution (1 M KBi, pH = 9.7) under AM 1.5 G illumination (100 mW/cm^2) from the back side. The electrodeposition time of PBA was optimized to obtain the best performance (Fig. S5). The photocurrent density of pure $BiVO_4$ is dramatically enhanced by the cocatalysts. As shown in Fig. 3(a), N-CFO/BVO exhibits a photocurrent of 4.83 mA/cm^2 at 1.23 V *vs.* RHE, about 4.13-fold of the photocurrent density of BVO (1.17 mA/cm^2). As listed in Table S1, the performance of N-CFO/BVO electrode exceeds most of the reported $BiVO_4$ photoanodes coupled with Co and/or Fe based cocatalysts. By contrast, CFO/BVO with O vacancy shows a photocurrent density of 4.38 mA/cm^2. This improvement should be attributed to N incorporation, which mends the lattice distortion in an oxygen-vacancy-rich cobalt-iron oxide since N atoms have almost the same diameter (0.75 Å) with O atoms (0.74 Å)[46]. For comparison, the pristine $BiVO_4$ sample annealed under N_2 atmosphere (denoted as N-BVO, green line in Fig. 3(a)) shows a declined performance of merely 0.66 mA/cm^2 at 1.23 V_{RHE}, implying that the inappropriate N doping into $BiVO_4$ may damage its intrinsic performance. Moreover, the onset potentials of N-CFO/BVO and CFO/BVO are about 0.36 V_{RHE}. A large cathodically shift of the onset potential of ~370 mV is observed as a proof of the cocatalytic function of the cobalt-iron oxide species. This shift is larger than most of similar cocatalysts reported in previous literatures, as given in Table S1. Under chopped light illumination (Fig. S6(a)), when the light is turned on, the transient spikes are eliminated since the cocatalyst layers can reduce the charge recombination at the interface [47]. Both N-CFO/BVO and CFO/BVO exhibit enhanced incident photon-to-current efficiencies (IPCE) in the range of 360–520 nm, as shown in Fig. 3(b). The IPCE values of the pristine BVO film are lower than 30% in the whole photo-responsive range, while the highest efficiency of N-CFO/BVO and CFO/BVO reaches 87% and 76% at 370 nm, respectively.

Furthermore, the N-CFO/BVO film also exhibits slower performance degradation under constant potential than CFO/BVO (Fig. S6(b)). The morphology and crystalline phases remain the same after the stability measurement, as shown in Fig. S7 and S8. XPS measurement was carried out to figure out the reason of photocurrent degradation in N-CFO/BVO. As shown in Fig. S9, it can be observed that the N 1s peak is weakened after the stability test. The atomic ratio of N/Bi decreases from 0.61 to 0.24 corresponding to the sample before and after stability test, respectively. From literatures, it is known the transitional metal based electrocatalysts always suffer from poor stability due to the dissolution of metal atoms [48,49]. According to XPS element analysis, the ratios of Co/Bi and Fe/Bi in this work also show a slight reduction as listed in Table S2. Therefore, the photocurrent loss of N-CFO/BVO can be attributed to the oxidation of N dopant and the loss of Co and Fe ions. The gas evolution of N-CFO/BVO during stability test was recorded by a gas chromatography. As shown in Fig. S10, the measured gas evolutions of H_2 and O_2 are fitted well with the calculated values and a high overall faradaic efficiency over 95% is calculated, which proves that the photogenerated electrons and holes are used for splitting water into H_2 and O_2.

To understand the influence of the incorporation of N atoms, the optical property of three samples was investigated first. As shown in Fig. 3(c), the BVO film possesses a light absorption edge of ~520 nm, which is unchanged after the deposition of cocatalysts. According to the UV-Vis spectra and Tauc plots (Fig. S11(a)), all three samples possess a band gap of 2.51 eV. However, both two cocatalyst layers increase light harvesting of BVO between 350 and 470 nm. Moreover, compared to CFO/BVO, the N-CFO/BVO electrode exhibits a tail absorption band at 520–600 nm, which may result from the N impurity level. But this extension of the light absorption will not contribute to the photocurrent enhancement since the IPCE curves reveal that the photo-responsive range of the electrodes is smaller than 520 nm. To compare the bulk charge separation efficiency η_{sep}, we also measured in a 1 M potassium borate electrolyte with 0.2 M Na_2SO_3 as a hole scavenger. As shown in Fig. S11(b), the *J-V* curves of N-CFO/BVO and CFO/BVO films nearly overlap. Therefore, the performance enhancement from CFO/BVO to N-CFO/BVO should not be attributed to light harvesting and bulk charge separation.

The surface charge transfer efficiency can be calculated from the *J-V* curves measured in KBi electrolyte without and with a hole scavenger. The result is given in Fig. 3(d). The charge transfer efficiency of the BVO film is lower than 40% due to the sluggish reaction kinetic, which can be greatly enhanced by a cocatalyst layer. N-CFO/BVO shows highest charge transfer efficiency. At 1.23 V_{RHE}, η_{trans} of N-CFO/BVO is 76.9%, about 1.13 folds of CFO/BVO. Therefore, the 10% increment of the photocurrent of N-CFO/BVO to CFO/BVO mainly results from the surface charge transfer enhancement. In addition, electrochemical impedance spectroscopy (EIS) was employed. The semicircle diameter in EIS Nyquist plot can be used to compare charge transfer resistance. As shown in Fig. 3(e), the N-CFO/BVO film demonstrates the smallest semicircle. These curves are fitted using the equivalent circuit model given in Fig. S12 and the fitted results are listed in Table S3. The calculated R_{ct} of N-CFO/BVO is about 17.0 kΩ, much smaller than CFO/BVO and BVO. According to these results, we can conclude that the N-doped cobalt-iron oxide cocatalyst layer has higher OER activity and accelerated charge transfer at the electrode/electrolyte interface.

Mott-Schottky (MS) curves of the BVO, CFO/BVO and N-CFO/BVO were measured as given in Fig. 3(f). All three electrodes exhibit a positive slope, which is evidence of *n*-type semiconductor. Compared with BVO, MS curves of CFO/BVO and N-CFO/BVO possess a smaller slope. Thus, according to Eq. (2) (Experimental Section), the donor densities of N-CFO/BVO and CFO/BVO are larger than the pristine BVO. The increased donor concentration can be attributed to the abundant defects in cocatalyst layers. The flat band potential (V_{FB}) shift to higher potential in CFO/BVO proves the formation of *p-n* junction between CFO and BVO [3], which may decrease photovoltage. In contrast, although the N-CFO/BVO electrode exhibits moderate carrier concentration (~2.20 $\times 10^{21}$ cm^{-3}), its V_{FB} shifts back to low potential, therefore, CFO/BVO and N-CFO/BVO show similar onset potential in *J-V* curves. Both *J-V* curves measured in the light and dark imply that N-CFO/BVO exhibits higher photocurrent densities at higher applied voltage, as shown in Fig. 3(a) and Fig. S13. The *J-V* curves measured in the dark (Fig. S13) show that N-CFO/BVO exhibits lower overpotential to achieve a current density of 10 mA/cm^2 and steeper water oxidation current density curve than CFO/BVO.

3.3. Density functional theory (DFT) calculations

To further reveal the mechanism, density functional theory (DFT) calculations were employed, as shown in Fig. 4. The band structure and density of states (DOS) of $CoFe_2O_4$ were first calculated. The band gap of $CoFe_2O_4$ between conduction band minimum (CBM) and valence band maximum (VBM) is about 1.50 eV. Both oxygen vacancy and nitrogen substitution decrease the band gap of $CoFe_2O_4$. In addition, N defects
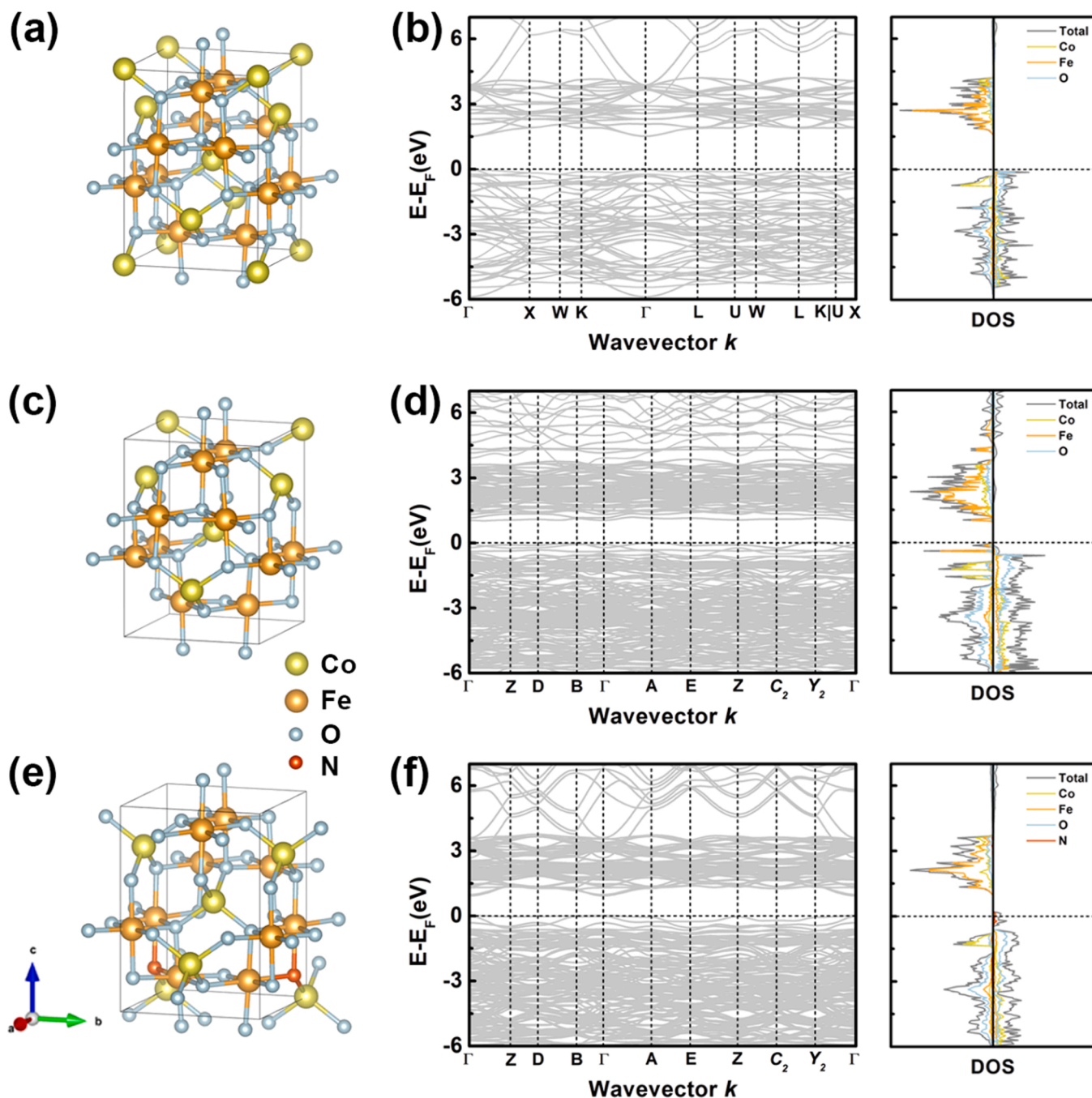
Fig. 4. Optimized structures, DFT calculated band structure and density of states spectra of (a, b) CoFe$_2$O$_4$, (c, d) CoFe$_2$O$_4$ with oxygen vacancy and (e, f) CoFe$_2$O$_4$ with nitrogen substitution.

introduce an impurity level in the band gap, which is in good agreement with the tail absorption band of N-CFO/BVO appeared in UV-Vis curves in Fig. 3(c). Moreover, the DOS at the Fermi level of N-substituted CoFe$_2$O$_4$ is nonzero, therefore endowing it metallic characteristic [13]. These results prove that N doping inherited from the N-rich PBA precursor renders cobalt-iron oxide higher electrical conductivity and helps charge transfer across the cocatalyst layer, especially under high applied voltage.

Nevertheless, owing to the ultrathin nature of cocatalyst layers (generally thinner than 10 nm), the effect of electrical conductivity is finite [39,50]. Therefore, the activation of OER ability of cocatalysts is also emphasized. Cyclic voltammetry (CV) curves were measured to determine the electrochemical active surface areas (ECSA) of three samples, given in Fig. S14. Because of the ultrathin and compact nature,

the ECSA of BVO shows little change after the deposition of cocatalyst and the CFO/BVO and N-CFO/BVO electrodes have similar ECSA values. The enhanced activity of N-CFO should be attributed to the activation of individual catalytic center, instead of the increased number of active sites. To further evaluate the OER catalytic activity, the Gibbs free energy at zero potential is calculated, as shown in Fig. 5. The four-electron oxygen evolution reaction can be decomposed into four steps with the intermediates of * , *OH, *O and *OOH [51], as described in Eqs. (3)–(6) (Experimental Section). The free energy diagram of both CoFe$_2$O$_4$ with oxygen vacancy and nitrogen substitution demonstrate that the third step (*O + H$_2$O → *OOH + e$^-$ + H$^+$) is the rate-determining step with largest energy barrier. The overpotential of N-CFO/BVO is 0.68 eV, which is much smaller than CFO/BVO (2.53 eV). It is obvious evidence of the enhanced catalytic activity of N-CFO/BVO, which results from the
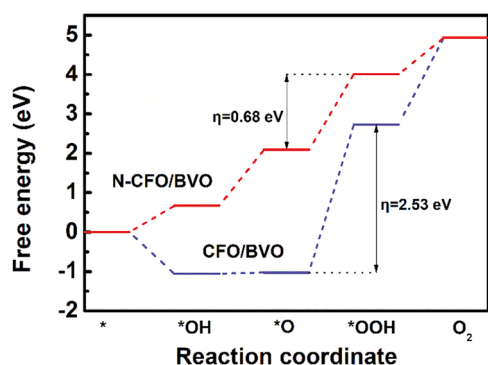
Fig. 5. Free-energy diagram for OER pathway on N-CFO/BVO and CFO/BVO.

activation ability of N doping. However, the activity of N-CFO is probably limited by its surface hydrophilicity. As Fig. 5 suggests, the *OH-(CFO/BVO) intermediate is thermodynamically more stable than *OH-(N-CFO/BVO) because of its lower free energy [9]. Therefore, the affinity of CFO/BVO with OH$^-$ in water is higher, implying higher surface wettability, which is further verified by contact angle test. As shown in Fig. S15, the contact angle of CFO/BVO is 10.8°, smaller than that of N-CFO/BVO (22.5°).

Based on the above results, a possible mechanism is proposed as illustrated in Fig. 6. Taking oxygen vacancy as a reference, the effects of nitrogen substitution are evaluated from both experimental and theoretical aspects. Both two anion defects enhance the electrical conductivity of the cocatalysts. But considering the ultrathin thickness of the layer, the reaction activity should also be emphasized. Compared to O vacancies, N dopants not only provide better electrical conductivity, but also boost the OER catalytic activity of transition metal atoms, which is not limited by the thickness and crystallinity of cocatalyst layer. The activity of metal atoms originates from the change of valence states [19,

39] and their activation results from the augment of electron density of Co and Fe, as implied in the XPS spectra in Fig. 2(c) and (d). During the reaction process, the electron-rich atoms in N-CFO/BVO attract holes and undergo valence change, thus promote the surface reaction and accelerate surface OER kinetic. Therefore, N dopants may be a more effective defect to boost the activity of cocatalysts for PEC water splitting than that of O vacancies.

3.4. Composition diversity of cocatalysts

Since there is a large family of Prussian blue analogues (PBAs), PBAs with other transitional metals (*e.g.*, Ni, Zn) can also be synthesized through a simple modification of experimental details. To further demonstrated the composition diversity of cocatalysts prepared by this strategy, nickel-iron oxides (NFO) and iron oxides (FO) annealed in N_2 and air were successfully synthesized onto $BiVO_4$ photoanodes through a simple modification of electrodepostion process. Therefore, the method reported here is a general and facile method for the synthesis of transitional-metal-based cocatalysts with variable constituents.

The PEC performance measured in 1 M KBi electrolyte is given in Fig. S16. All four photoanodes exhibit higher photocurrent densities at 1.23 V_{RHE} and decreased onset potentials than bare BVO photoanode. Compared with those annealed in the air, N-NFO/BVO and N-FO/BVO treated in N_2 atmosphere show higher performances, same with the results in cobalt-iron oxides. The roles of different transitional metal ions for enhancing the PEC performances can also be discussed as below. Compared with those mixed with cobalt and nickel, N-FO/BVO and FO/BVO exhibit lower performances, which is consistent with the reported observation in transitional-metal-based electrocatalysts [52]. Generally, pristine iron oxides have lower OER activity than cobalt or nickel oxides because of their poor electrical conductivity. However, the performance can be greatly enhanced when Fe is mixed with Co or Ni. As shown in Fig. 3(a) and Fig. S16, the photocurrent densities of both CFO/BVO and NFO/BVO are higher than that of FO/BVO. It is believed that the
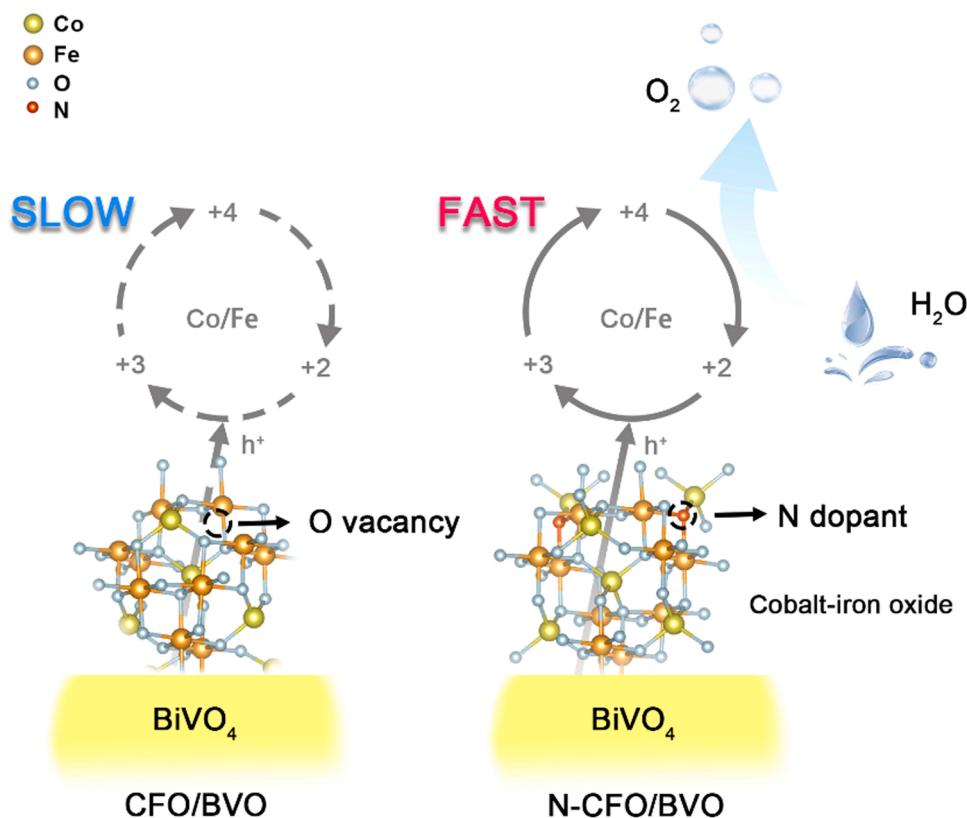

Fig. 6. Schematic illustration of PEC reaction on CFO/BVO and N-CFO/BVO photoanodes.

introduction of Fe atoms would provide abundant active sites to these transitional-metal cocatalysts [39]. In addition, because of the difference of valence states, dual metal cocatalysts also have more defects [3], which can also boost the OER activity.

4. Conclusions

In conclusion, we presented the feasibility of employing Prussian blue analogue as a precursor for the preparation of a new metal oxide cocatalyst. An ultrathin layer of nitrogen-doped cobalt-iron dual metal oxide cocatalyst (N-CFO) was decorated onto BVO electrode by annealing under a mild N_2 atmosphere. As a result of the excellent OER ability of N-CFO, the photocurrent density of the N-CFO/BVO photoanode is remarkably promoted to 4.83 mA/cm^2 at 1.23 V$_{RHE}$ under AM 1.5 G illumination, about 4.13-fold of pure BiVO$_4$, and the onset potential is cathodically shifted to 0.36 V$_{RHE}$. The intrinsic mechanism of performance improvement is carefully investigated. Detailed experimental results show that the cocatalyst greatly facilitates the surface charge transfer efficiency and XPS spectra exhibit that the N incorporation effectively modulates the electronic configuration around Co and Fe atoms. Computational investigation further confirms that the N dopants not only improve the electrical conductivity, but also activate the catalytic centers, which are beneficial to the catalytic performance. This work not only reveals the impact of N incorporation, but also provides a new strategy to design the chemical composition of cocatalysts for high-efficiency PEC photoanodes: the diversity of PBAs guarantees the compositional tunability of the final product and the electrodeposition process strengthens interfacial electrochemical contact between cocatalyst and BiVO$_4$.

CRediT authorship contribution statement

Jingyi Lin: Investigation, Methodology, Formal analysis, Visualization, Validation, Writing – original draft. **Xiujun Han:** Software, Visualization, Data curation. **Siyuan Liu:** Investigation. **Ying Lv:** Resources. **Xin Li:** Validation. **Yixin Zhao:** Supervision. **Yao Li:** Supervision. **Lianzhou Wang:** Supervision, Conceptualization, Writing – review & editing. **Shenmin Zhu:** Supervision, Conceptualization, Writing – review & editing, Project administration, Funding acquisition.

Declaration of Competing Interest

The authors declare that they have no known competing financial interests or personal relationships that could have appeared to influence the work reported in this paper.

Data availability

Data will be made available on request.

Appendix A. Supporting information

Supplementary data associated with this article can be found in the online version at doi:10.1016/j.apcatb.2022.121947.

References

[1] C. Jiang, S.J.A. Moniz, A. Wang, T. Zhang, J. Tang, Photoelectrochemical devices for solar water splitting - materials and challenges, Chem. Soc. Rev. 46 (2017) 4645–4660.

[2] Y. Kuang, T. Yamada, K. Domen, Surface and interface engineering for photoelectrochemical water oxidation, Joule 1 (2017) 290–305.

[3] S.C. Wang, T.W. He, J.H. Yun, Y.X. Hu, M. Xiao, A.J. Du, L.Z. Wang, New iron-cobalt oxide catalysts promoting BiVO4 films for photoelectrochemical water splitting, Adv. Funct. Mater. 28 (2018), 1802685.

[4] K. Sivula, R. van de Krol, Semiconducting materials for photoelectrochemical energy conversion, Nat. Rev. Mater. 1 (2016) 15010.

[5] Q. Sun, T. Cheng, Z.R. Liu, L.M. Qi, A cobalt silicate modified BiVO4 photoanode for efficient solar water oxidation, Appl. Catal. B Environ. 277 (2020), 119189.

[6] H. He, A. Liao, W. Guo, W. Luo, Y. Zhou, Z. Zou, State-of-the-art progress in the use of ternary metal oxides as photoelectrode materials for water splitting and organic synthesis, Nano Today 28 (2019), 100763.

[7] C. Ding, J. Shi, Z. Wang, C. Li, Photoelectrocatalytic water splitting: significance of cocatalysts, electrolyte, and interfaces, ACS Catal. 7 (2016) 675–688.

[8] F.S. Li, H. Yang, Q.M. Zhuo, D.H. Zhou, X.J. Wu, P.L. Zhang, Z.Y. Yao, L.C. Sun, A cobalt@cucurbit[5]uril complex as a highly efficient supramolecular catalyst for electrochemical and photoelectrochemical water splitting, Angew. Chem. Int. Ed. 60 (2021) 1976–1985.

[9] J.B. Pan, B.H. Wang, J.B. Wang, H.Z. Ding, W. Zhou, X. Liu, J.R. Zhang, S. Shen, J. K. Guo, L. Chen, C.T. Au, L.L. Jiang, S.F. Yin, Activity and stability boosting of an oxygen-vacancy-rich BiVO4 photoanode by NiFe-MOFs thin layer for water oxidation, Angew. Chem. Int. Ed. 60 (2021) 1433–1440.

[10] K.J. McDonald, K.S. Choi, Photodeposition of Co-based oxygen evolution catalysts on alpha-Fe2O3 photoanodes, Chem. Mater. 23 (2011) 1686–1693.

[11] D.K. Zhong, S. Choi, D.R. Gamelin, Near-complete suppression of surface recombination in solar photoelectrolysis by "Co-Pi" catalyst-modified W:BiVO4, J. Am. Chem. Soc. 133 (2011) 18370–18377.

[12] J.C. Liu, J.M. Li, Y.F. Li, J. Guo, S.M. Xu, R.K. Zhang, M.F. Shao, Photoelectrochemical water splitting coupled with degradation of organic pollutants enhanced by surface and interface engineering of BiVO4 photoanode, Appl. Catal. B Environ. 278 (2020), 119268.

[13] D. He, R.T. Gao, S.J. Liu, M. Sun, X.H. Liu, K. Hu, Y.G. Su, L. Wang, Yttrium-induced regulation of electron density in NiFe layered double hydroxides yields stable solar water splitting, ACS Catal. 10 (2020) 10570–10576.

[14] T.W. Kim, K.S. Choi, Nanoporous BiVO4 photoanodes with dual-layer oxygen evolution catalysts for solar water splitting, Science 343 (2014) 990–994.

[15] P.F. Yue, H.D. She, L. Zhang, B. Niu, R. Lian, J.W. Huang, L. Wang, Q.Z. Wang, Super-hydrophilic CoAl-LDH on BiVO4 for enhanced photoelectrochemical water oxidation activity, Appl. Catal. B Environ. 286 (2021), 119875.

[16] D. Cardenas-Morcoso, R. Ifraemov, M. Garcia-Tecedor, I. Liberman, S. Gimenez, I. Hod, A metal-organic framework converted catalyst that boosts photo-electrochemical water splitting, J. Mater. Chem. A 7 (2019) 11143–11149.

[17] J.Y. Liu, Z.D. Wei, W.F. Shangguan, Defects engineering in photocatalytic water splitting materials, ChemCatChem 11 (2019) 6177–6189.

[18] G. Ge, M. Liu, C. Liu, W. Zhou, D.F. Wang, L.Q. Liu, J.H. Ye, Ultrathin FeOOH nanosheets as an efficient cocatalyst for photocatalytic water oxidation, J. Mater. Chem. A 7 (2019) 9222–9229.

[19] S.Q. Zhou, K.Y. Chen, J.W. Huang, L. Wang, M.Y. Zhang, B. Bai, H. Liu, Q.Z. Wang, Preparation of heterometallic CoNi-MOFs-modified BiVO4: a steady photoanode for improved performance in photoelectrochemical water splitting, Appl. Catal. B Environ. 266 (2020), 118513.

[20] T. Feng, X.R. Zhao, C.K. Dong, H. Liu, X.W. Du, J. Yang, Boosting reversible oxygen electrocatalysis with enhanced interfacial pyridinic-N-Co bonding in cobalt oxide/mesoporous N-doped graphene hybrids, Nanoscale 10 (2018) 22140–22147.

[21] J.H. Hao, W.S. Yang, Z. Peng, C. Zhang, Z.P. Huang, W.D. Shi, A nitrogen doping method for CoS2 electrocatalysts with enhanced water oxidation performance, ACS Catal. 7 (2017) 4214–4220.

[22] J.F. Xie, Y. Xie, Transition metal nitrides for electrocatalytic energy conversion: opportunities and challenges, Chem. - Eur. J. 22 (2016) 3588–3598.

[23] F. Lu, M. Zhou, Y.X. Zhou, X.H. Zeng, First-row transition metal based catalysts for the oxygen evolution reaction under alkaline conditions: basic principles and recent advances, Small 13 (2017), 1701931.

[24] N. Han, P.Y. Liu, J. Jiang, L.H. Ai, Z.P. Shao, S.M. Liu, Recent advances in nanostructured metal nitrides for water splitting, J. Mater. Chem. A 6 (2018) 19912–19933.

[25] H.M. Sun, Z.H. Yan, F.M. Liu, W.C. Xu, F.Y. Cheng, J. Chen, Self-supported transition-metal-based electrocatalysts for hydrogen and oxygen evolution, Adv. Mater. 32 (2020), 1806326.

[26] X.Z. Song, S.Y. Song, D. Wang, H.J. Zhang, Prussian blue analogs and their derived nanomaterials for electrochemical energy storage and electrocatalysis, Small, Methods 5 (2021), 2001000.

[27] L. Han, X.Y. Yu, X.W. Lou, Formation of Prussian-blue-analog nanocages via a direct etching method and their conversion into Ni-Co-mixed oxide for enhanced oxygen evolution, Adv. Mater. 28 (2016) 4601–4605.

[28] Y. Hou, T.Z. Huang, Z.H. Wen, S. Mao, S.M. Cui, J.H. Chen, Metal-organic framework-derived nitrogen-doped core-shell-structured porous Fe/Fe3C@C nanoboxes supported on graphene sheets for efficient oxygen reduction reactions, Adv. Energy Mater. 4 (2014), 1400337.

[29] G. Kresse, J. Furthmüller, Efficient iterative schemes for ab initio total-energy calculations using a plane-wave basis set, Phys. Rev. B 54 (1996) 11169–11186.

[30] V. Wang, N. Xu, J.C. Liu, G. Tang, W.T. Geng, VASPKIT: A user-friendly interface facilitating high-throughput computing and analysis using VASP code, Comput. Phys. Commun. 267 (2021), 108033.

[31] Y.C. Fan, S. Ida, A. Staykov, T. Akbay, H. Hagiwara, J. Matsuda, K. Kaneko, T. Ishihara, Ni-Fe nitride nanoplates on nitrogen-doped graphene as a synergistic catalyst for reversible oxygen evolution reaction and rechargeable Zn-air battery, Small 13 (2017), 1700099.

[32] Y.W. Hu, D. Huang, J.N. Zhang, Y.C. Huang, M.S.J.T. Balogun, Y.X. Tong, Dual doping induced interfacial engineering of Fe_2N/Fe_3N hybrids with favorable d-band towards efficient overall water splitting, ChemCatChem 11 (2019) 6051–6060.

[33] S.A. Carminati, B.L. da Silva, J.L. Bott-Neto, M.A. de Melo, M.T. Galante, P. S. Fernandez, C. Longo, J.A. Bonacin, A.F. Nogueira, Hematite nanorods photoanodes decorated by cobalt hexacyanoferrate: the role of mixed oxidized states on the enhancement of photoelectrochemical performance, ACS Sustain. Chem. Eng. 3 (2020) 10097–10107.

[34] A. Bordage, R. Moulin, E. Fonda, G. Fornasieri, E. Riviere, A. Bleuzen, Evidence of the core-shell structure of (photo)magnetic CoFe Prussian blue analogue nanoparticles and peculiar behavior of the surface species, J. Am. Chem. Soc. 140 (2018) 10332–10343.

[35] Q.J. Meng, B.B. Zhang, L.Z. Fan, H.D. Liu, M. Valvo, K. Edstrom, M. Cuartero, R. de Marco, G.A. Crespo, L.C. Sun, Efficient $BiVO_4$ photoanodes by postsynthetic treatment: remarkable improvements in photoelectrochemical performance from facile borate modification, Angew. Chem. Int. Ed. 58 (2019) 19027–19033.

[36] X. Zhong, L. Liu, Y. Jiang, X. Wang, L. Wang, G. Zhuang, X. Li, D. Mei, J.-G. Wang, D.S. Su, Synergistic effect of nitrogen in cobalt nitride and nitrogen-doped hollow carbon spheres for the oxygen reduction reaction, ChemCatChem 7 (2015) 1826–1832.

[37] D.W. Su, M. Cortie, G.X. Wang, Fabrication of N-doped graphene-carbon nanotube hybrids from Prussian blue for lithium-sulfur batteries, Adv. Energy Mater. 7 (2017), 1602014.

[38] K. Zhang, G. Zhang, J.H. Qu, H.J. Liu, Disordering the atomic structure of Co(II) oxide via B-doping: an efficient oxygen vacancy introduction approach for high oxygen evolution reaction electrocatalysts, Small 14 (2018), 1802760.

[39] C.C. Feng, Q. Zhou, B. Zheng, X. Cheng, Y.J. Zhang, Y.P. Bi, Ultrathin $NiCo_2O_4$ nanosheets with dual-metal active sites for enhanced solar water splitting of a $BiVO_4$, Photo, J. Mater. Chem. A 7 (2019) 22274–22278.

[40] Y. Ma, J.T. Li, X.B. Liao, W. Luo, W.Z. Huang, J.S. Meng, Q. Chen, S.B. Xi, R.H. Yu, Y. Zhao, L. Zhou, L.Q. Mai, Heterostructure design in bimetallic phthalocyanine boosts oxygen reduction reaction activity and durability, Adv. Funct. Mater. 30 (2020), 2005000.

[41] B.B. Zhang, S.Q. Yu, Y. Dai, X.J. Huang, L.J. Chou, G.X. Lu, G.J. Dong, Y.P. Bi, Nitrogen-incorporation activates $NiFeO_x$ catalysts for efficiently boosting oxygen evolution activity and stability of $BiVO_4$ photoanodes, Nat. Commun. 12 (2021) 6969.

[42] S. Feng, T. Wang, B. Liu, C. Hu, L. Li, Z.J. Zhao, J. Gong, Enriched surface oxygen vacancies of photoanodes by photoetching with enhanced charge separation, Angew. Chem. Int. Ed. 59 (2020) 2044–2048.

[43] T.W. Kim, Y. Ping, G.A. Galli, K.S. Choi, Simultaneous enhancements in photon absorption and charge transport of bismuth vanadate photoanodes for solar water splitting, Nat. Commun. 6 (2015) 8769.

[44] S. Sriwichai, R. Irani, F.X. Xi, D. Friedrich, C. Hohn, I.Y. Ahmet, N. Wetchakun, F. F. Abdi, Role of Gd in enhancing the charge carrier mobility of spray-deposited $BiVO_4$ photoanodes, Sol. RRL 5 (2021), 2100268.

[45] Y. Lu, J. Su, J. Shi, D. Zhou, Surface recombination passivation of the $BiVO_4$ photoanode by the synergistic effect of the cobalt/nickel sulfide cocatalyst, ACS Appl. Energy Mater. 3 (2020) 9089–9097.

[46] H.H. Wu, D.Y. Yang, X.H. Zhu, P. Gu, H. Sun, P.H. Wangyang, J.T. Li, X.D. He, L. J. Fan, Effect of the nitrogen-oxygen ratio on the position of N atoms in the TiO_2 lattice of N-doped TiO_2 thin films prepared by DC magnetron sputtering, CrystEngComm 20 (2018) 4133–4140.

[47] F. Le Formal, K. Sivula, M. Gratzel, The transient photocurrent and photovoltage behavior of a hematite photoanode under working conditions and the influence of surface treatments, J. Phys. Chem. C. 116 (2012) 26707–26720.

[48] R. Chen, S.F. Hung, D.J. Zhou, J.J. Gao, C.J. Yang, H.B. Tao, H.B. Yang, L.P. Zhang, L.L. Zhang, Q.H. Xiong, H.M. Chen, B. Liu, Layered structure causes bulk NiFe layered double hydroxide unstable in alkaline oxygen evolution reaction, Adv. Mater. 31 (2019), 1903909.

[49] C.G. Kuai, Z.R. Xu, C. Xi, A.Y. Hu, Z.J. Yang, Y. Zhang, C.J. Sun, L.X. Li, D. Sokaras, C.K. Dong, S.Z. Qiao, X.W. Du, F. Lin, Phase segregation reversibility in mixed-metal hydroxide water oxidation catalysts, Nat. Catal. 3 (2020) 743–753.

[50] M. Zhong, T. Hisatomi, Y.B. Kuang, J. Zhao, M. Liu, A. Iwase, Q.X. Jia, H. Nishiyama, T. Minegishi, M. Nakabayashi, N. Shibata, R. Niishiro, C. Katayama, H. Shibano, M. Katayama, A. Kudo, T. Yamada, K. Domen, Surface modification of CoO_x loaded $BiVO_4$ photoanodes with ultrathin p-type NiO layers for improved solar water oxidation, J. Am. Chem. Soc. 137 (2015) 5053–5060.

[51] J. Rossmeisl, A. Logadottir, J.K. Norskov, Electrolysis of water on (oxidized) metal surfaces, Chem. Phys. 319 (2005) 178–184.

[52] M.Q. Yu, E. Budiyanto, H. Tuysuz, Principles of water electrolysis and recent progress in cobalt-, nickel-, and iron-based oxides for the oxygen evolution reaction, Angew. Chem. Int. Ed. 61 (2022), e202103824.